AGU PUBLICATIONS

JGR

Journal of Geophysical Research: Space Physics

RESEARCH ARTICLE

10.1002/2014JA020863

Special Section:
New perspectives on Earth's radiation belt regions from the prime mission of the Van Allen Probes

Key Points:

- We report conjugate space-ground observations for an undulation event
- The auroral undulations concur with second harmonic poloidal waves
- A common periodic signature is found in the conjugate aurora and magnetosphere

Supporting Information:

- Text S1
- Movie S1

Correspondence to:
T. Motoba,
tetsuo.motoba@gmail.com

Citation:
Motoba, T., et al. (2015), Link between premidnight second harmonic poloidal waves and auroral undulations: Conjugate observations with a Van Allen Probe spacecraft and a THEMIS all-sky imager, *J. Geophys. Res. Space Physics*, *120*, 1814–1831, doi:10.1002/2014JA020863.

Received 21 NOV 2014
Accepted 13 FEB 2015
Accepted article online 16 FEB 2015
Published online 18 MAR 2015

Link between premidnight second harmonic poloidal waves and auroral undulations: Conjugate observations with a Van Allen Probe spacecraft and a THEMIS all-sky imager

T. Motoba[1], K. Takahashi[1], A. Ukhorskiy[1], M. Gkioulidou[1], D. G. Mitchell[1], L. J. Lanzerotti[2], G. I. Korotova[3,4], E. F. Donovan[5], J. R. Wygant[6], C. A. Kletzing[7], W. S. Kurth[7], and J. B. Blake[8]

[1]Johns Hopkins University Applied Physics Laboratory, Laurel, Maryland, USA, [2]New Jersey Institute of Technology, Newark, New Jersey, USA, [3]IZMIRAN, Troitsk, Russia, [4]IPST, University of Maryland, College Park, Maryland, USA, [5]Physics and Astronomy Department, University of Calgary, Calgary, Alberta, Canada, [6]School of Physics and Astronomy, University of Minnesota, Minneapolis, Minnesota, USA, [7]Department of Physics and Astronomy, University of Iowa, Iowa City, Iowa, USA, [8]The Aerospace Corporation, Los Angeles, California, USA

Abstract We report, for the first time, an auroral undulation event on 1 May 2013 observed by the Time History of Events and Macroscale Interactions During Substorms (THEMIS) all-sky imager (ASI) at Athabasca ($L = 4.6$), Canada, for which in situ field and particle measurements in the conjugate magnetosphere were available from a Van Allen Probe spacecraft. The ASI observed a train of auroral undulation structures emerging spontaneously in the premidnight subauroral ionosphere during the growth phase of a substorm. The undulations had an azimuthal wavelength of ~180 km and propagated westward at a speed of 3–4 km s^{-1}. The successive passage over an observing point yielded quasiperiodic oscillations in diffuse auroral emissions with a period of ~40 s. The azimuthal wave number m of the auroral luminosity oscillations was found to be $m \sim -103$. During the event, the spacecraft—being on tailward stretched field lines ~0.5 R_E outside the plasmapause that mapped into the ionosphere conjugate to the auroral undulations—encountered intense poloidal ULF oscillations in the magnetic and electric fields. We identify the field oscillations to be the second harmonic mode along the magnetic field line through comparisons of the observed wave properties with theoretical predictions. The field oscillations were accompanied by oscillations in proton and electron fluxes. Most interestingly, both field and particle oscillations at the spacecraft had one-to-one association with the auroral luminosity oscillations around its footprint. Our findings strongly suggest that this auroral undulation event is closely linked to the generation of second harmonic poloidal waves.

1. Introduction

Undulation on the equatorward boundary of the diffuse aurora is a characteristic auroral structure that occasionally develops at duskside subauroral latitudes mostly during geomagnetically active periods. Auroral undulations provide a unique opportunity to visualize instabilities occurring in the magnetosphere.

The first observations of auroral undulations were reported by *Lui et al.* [1982] with auroral images from the Defense Meteorological Satellite Program (DMSP) satellites. *Lui et al.* [1982] found that the undulations typically have an azimuthal wavelength of ~200–900 km, an amplitude of ~40–400 km, and a lifetime of ~0.5–3.5 h. Subsequent global-scale imaging observations of auroral undulations have been made by DMSP [*Zhang et al.*, 2005] and Polar/IMAGE spacecraft [*Lewis et al.*, 2005; *Henderson et al.*, 2010].

Similar auroral undulations have also been observed with ground-based all-sky imagers at subauroral latitudes [*Nishitani et al.*, 1994; *Baishev et al.*, 2012]. *Nishitani et al.* [1994] first reported an example of auroral undulations observed at the Antarctic subauroral station, Sanae (L~4.0). Recently, *Baishev et al.* [2012] identified 11 auroral undulation events in the long-term (1994–2008) all-sky TV camera records at a Russian subauroral station, Zhigansk (L~4.4). Both ground-based studies found similar properties including azimuthal wavelength (~100–300 km), amplitude (~50–150 km), and propagation velocity (~0.5–1.0 km s^{-1} in the duskward (westward) direction). The wavelength and amplitude are near the lower limit of those reported in the spacecraft studies referenced above, suggesting that the auroral undulations seen from space and ground are caused by a common source. Such ground-based optical observations are highly valuable because they enable us to determine the motion and structure of auroral undulations with high time and spatial resolutions that are not possible with spacecraft. Unfortunately, ground observations of auroral undulations at subauroral latitudes are very rare in part because they often suffer from sunlight interference as well as because they depend somewhat on favorable conditions for the formation of large-scale undulations [*Rich et al.*, 1980; *Zhang et al.*, 2005].

The generation mechanism of the auroral undulations remains unclear. A possible energy source conventionally suggested for the generation of auroral undulations is a flow shear-related instability (such as the Kelvin-Helmholtz instability (KHI)). This mechanism was originally suggested by *Lui et al.* [1982] and *Kelley* [1986] and subsequently supported by numerical simulations [*Yamamoto et al.*, 1993]. Using simultaneous auroral and ion drift observations on DMSP, *Zhang et al.* [2005] found both large ion drift velocity (>1 km s^{-1}) and velocity shear (>0.1 s^{-1}) within the diffuse auroral oval that are thought to be necessary conditions for the auroral undulations to occur.

As an alternative, some authors [*Lui et al.*, 1982; *Fedorovich*, 1988; *Lewis et al.*, 2005] proposed that a drift wave instability excited at the inner edge of the plasma sheet is responsible for auroral undulations. This mechanism was supported by a numerical simulation of *Lewis et al.* [2005], who predicted that density structures similar to the auroral undulations are generated on the inner edge of the plasma sheet by a kinetic drift wave driven by the ion pressure gradient.

To determine whether these (or other possible) mechanisms produce the auroral undulations, it is necessary to observe the state of the electromagnetic fields and plasma in the magnetosphere with a spacecraft that is magnetically conjugate to the aurora. To the best of our knowledge, such observations have not been reported.

In this paper, we report an auroral undulation event on 1 May 2013, which was observed by a Time History of Events and Macroscale Interactions during Substorms (THEMIS) all-sky imager when a Van Allen Probe spacecraft made fortuitous in situ observations of the fields and particles in a region that was geomagnetically conjugate to the undulations. The conjugate space-ground observations are important data that provide new insights into possible processes in the inner magnetosphere that are involved in the generation of auroral undulations. We demonstrate that the auroral undulations in the event analyzed herein were caused by a second harmonic poloidal wave that is proposed here as an alternative source of auroral undulations.

The paper is organized as follows. The next section describes the space- and ground-based instruments used in the study. Section 3 describes each of the ground and satellite observations and their comparisons. The observational results are discussed in section 4 followed by conclusions in section 5.

2. Data

The primary sources of data used in this paper are the THEMIS Ground Based Observatory (GBO) [*Mende et al.*, 2008] and probe B of the Van Allen Probes mission (also known as the Radiation Belt Storm Probes (RBSP)) [*Mauk et al.*, 2013].

Each of the THEMIS GBO stations has a set of white light all-sky imager (ASI, 3 s sampling) and fluxgate magnetometer (0.5 s sampling). In this study, the THEMIS GBO data set at Athabasca (ATHA, 54.7°N, 246.7°E; magnetic latitude (MLAT) = 62.2°N, magnetic local time (MLT) = UT–08:18, $L = 4.6$) in Canada was used. We also used data from the fluxgate magnetometer (1 s sampling) at Ministik Lake (MSTK, 53.4°N, 247.0°E; MLAT = 60.9°N, MLT = UT–08:14, $L = 4.2$), one of the sites of the Canadian Array for Realtime Investigations of Magnetic Activity (CARISMA) magnetometer array [*Mann et al.*, 2008]. Ministik Lake is the closest site to ATHA in CARISMA. Throughout this study, the magnetic coordinate system in the ionosphere was represented in Altitude Adjusted Corrected Geomagnetic coordinates [*Baker and Wing*, 1989].

The RBSP-B data include the following: fluxes of 10–500 keV hydrogen ions (protons) measured by the Radiation Belt Storm Probes Ion Composition Experiment (RBSPICE) [*Mitchell et al.*, 2013], fluxes of 30–500 keV electrons measured by the Magnetic Electron Ion Spectrometer (MagEIS) [*Blake et al.*, 2013], magnetic field (**B**) vectors measured by the Electric and Magnetic Field Instrument Suite and Integrated Science (EMFISIS) magnetometer instrument [*Kletzing et al.*, 2013], electron density determined from plasma wave spectra

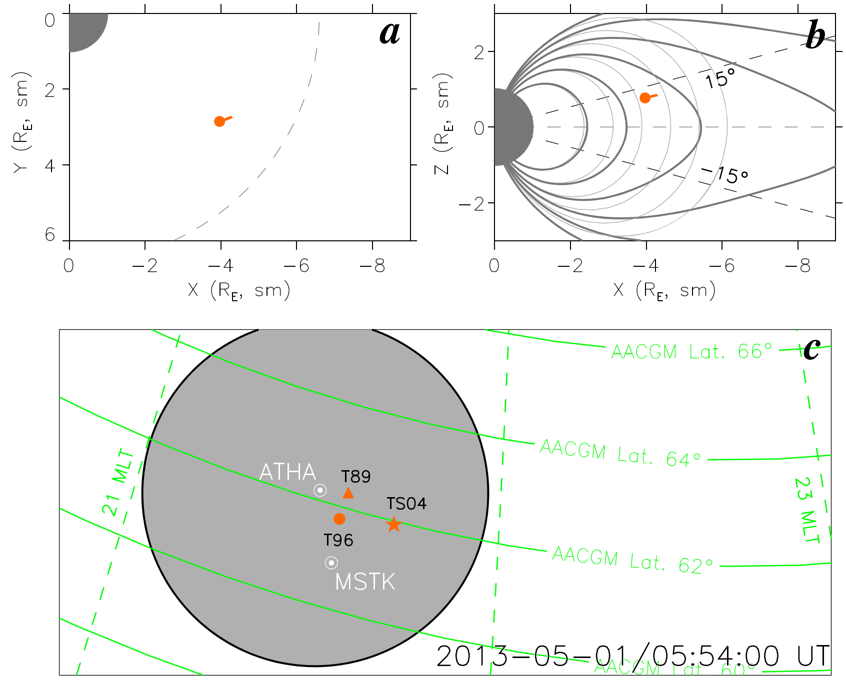

Figure 1. Position of the Van Allen Probe-B spacecraft in (a) the *x*-*y* plane and (b) the *x*-*z* plane in GSM coordinates from 05:45 to 06:00 UT on 1 May 2013. The heavy dot indicates the location at 05:45 UT. In the *x*-*z* plane, superimposed are the dipole field lines of $L = 3$–8 (light gray curves) and their stretched field lines (dark gray curves) expected from the T96 model (input parameters: $P_{sw} = 2.5$ nPa, $Dst = -20$ nT, IMF $B_y = -5.0$ nT, and IMF $B_z = -10.0$ nT) as a reference. (c) The orange-colored different shapes indicate the ionospheric footprints of the Van Allen Probe-B spacecraft deduced from three different Tsyganenko models (T89, T96, and TS04). The ASI field of view (elevation of ≲75°) at Athabasca (ATHA) projected to an altitude of 110 km is indicated, together with the Ministik Lake (MSTK) magnetometer station employed in this study.

measured by the EMFISIS Waves instrument, and electric field (**E**) vectors measured by the Electric Field and Waves (EFW) [*Wygant et al.*, 2013]. Note that in our analysis, an 11 s signal owing to the spin tone was removed with a low-pass filter from the EMFISIS magnetic field data. The electric field measurements were made in the spin plane of the spacecraft. The third component, directed along the satellite's spin axis (maintained at a small angle with respect to the Earth-Sun line), was derived using the assumption $\mathbf{E} \cdot \mathbf{B} = 0$. This technique is reliable when the magnetic field vector makes an angle greater than 20° from the spin plane, which was satisfied through the interval of interest.

The electric and magnetic field vector data used in the ULF wave analysis were rotated into the mean field-aligned (MFA) coordinate system. The MFA coordinate axes are taken along the direction of the unperturbed magnetic field (μ), radially outward (ν), and eastward (φ). When computing the cross spectra of data from different sources, we resampled the data at common time steps after an interpolation.

3. Observations

The conjugate observations of the RBSP-B spacecraft and THEMIS GBO at ATHA reported in the present study were made in the premidnight sector (~21:45 MLT) between 05:45 and 06:00 UT on 1 May 2013. The RBSP-B location in the *x*-*y* and *x*-*z* planes and its ionospheric footprint are presented in Figure 1. To estimate the ionospheric footprint, we here tested three different Tsyganenko magnetic field models, the Tsyganenko 1989 (T89) [*Tsyganenko*, 1989], Tsyganenko 1996 (T96) [*Tsyganenko and Stern*, 1996], and Tsyganenko and Sitnov 2004 (TS04) [*Tsyganenko and Sitnov*, 2005]. As seen in Figure 1c, the T96 model predicted the RBSP-B footprint to fall within ~50–80 km southeast of the zenith of ATHA (~62.2° MLAT). The T89 and TS04 footprints were broadly close to the T96 one within a radial distance of 50–120 km. Thus, any discrepancy between the Tsyganenko model fields is not significant for this event.

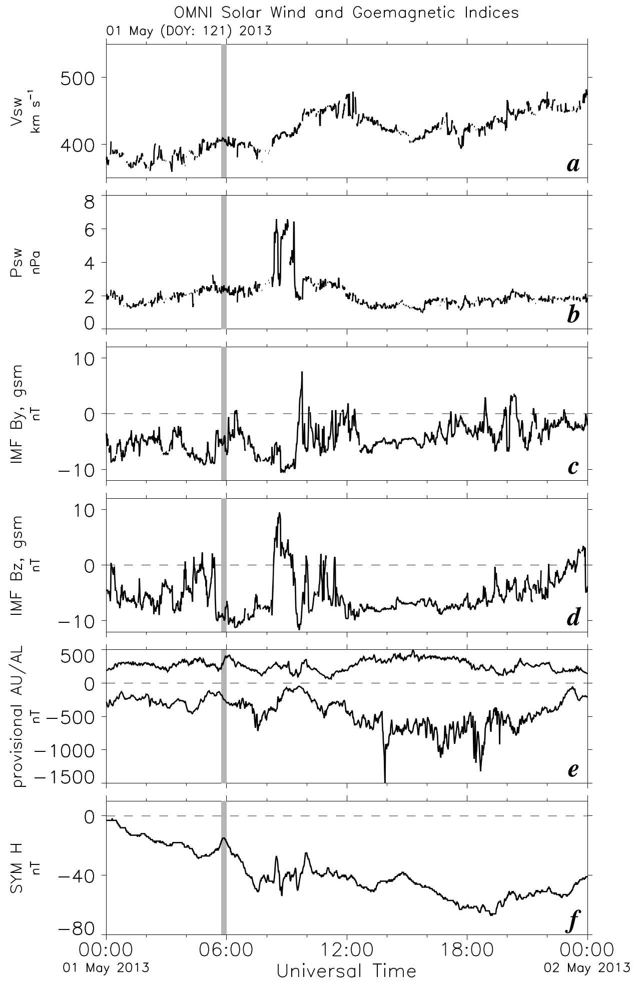

Figure 2. OMNI solar wind and geomagnetic indices on 1 May 2013. (a) The solar wind velocity, (b) solar wind dynamic pressure, (c) *y* component of interplanetary magnetic field (IMF B_y), (d) *z* component of IMF (IMF B_z), (e) provisional *AU* and *AL* indices, and (f) *SYM-H* index are shown from the top. The gray shading for 05:45–06:00 UT indicates the period when the interesting event was observed.

3.1. Geomagnetic and Solar Wind Conditions

Figure 2 presents an overview of upstream interplanetary magnetic field (IMF) and solar wind conditions for 1 May 2013, together with geomagnetic activity conditions. The IMF and solar wind conditions include the solar wind velocity (Figure 2a), solar wind dynamic pressure (Figure 2b), the B_y and B_z components of the IMF in GSM coordinates (Figures 2c and 2d, respectively), all obtained from the high-resolution (1 min) OMNI data. Geomagnetic activity conditions are illustrated by geomagnetic indices *AU* and *AL* (Figure 2e) and *SYM-H* (Figure 2f) obtained from the World Data Center (WDC) for Geomagnetism, Kyoto. These measurements are important in two key respects. First, they provide information on possible external energy input to the magnetosphere during the interval in question and on the resulting magnetospheric activity. Second, the upstream solar wind observations are used as input parameters for the magnetic field models to estimate the magnetic footprints of the RBSP-B satellite (as shown in Figure 1c). The gray shading indicates the period (05:45–06:00 UT) of the event studied here.

During the event, the solar wind velocity and dynamic pressure were almost steady with a value of ~400 km s^{-1} and ~2.5 nPa, respectively. The IMF B_y component basically stayed negative with strong perturbations between −10 and 0 nT. At 05:25 UT, the IMF B_z component turned from positive to negative and then the IMF B_z remained an almost constant value around −10 nT. In response to the negative excursion of the IMF B_z, as seen in Figure 2e, the *AU* (*AL*) indices began to increase (decrease) from ~200 to ~400 nT (from ~−150 to ~−300 nT), which would be regarded as a typical sign of the development of the substorm growth phase. It is also found in Figure 2f that the substorm growth phase was developing in the course of the main phase of a moderate geomagnetic storm (quick-look *Dst* reached the minimum value of −67 nT at 19:00 UT on 1 May). It is therefore concluded that the event took place under such geomagnetically active conditions.

3.2. Auroral Undulations

During the undulation event of interest, Athabasca (ATHA, ~62.2° MLAT) was in darkness just after sunset, allowing auroral observations of the subauroral region (while relatively rare) to be made. We also note that while ATHA had slightly cloudy skies in a small area of the field of view, the clouds had little effect on the optical analysis.

In response to the southward turning of the IMF, a growth phase arc was present in the poleward part (64°–66° MLAT) of the ASI field of view at ATHA and then it shifted gradually equatorward. After 05:40 UT, faint, unstructured (i.e., diffuse type) auroral undulations appeared just equatorward of the growth phase arc and propagated westward. As time passed, the auroral undulation structure approached the zenith of ATHA.

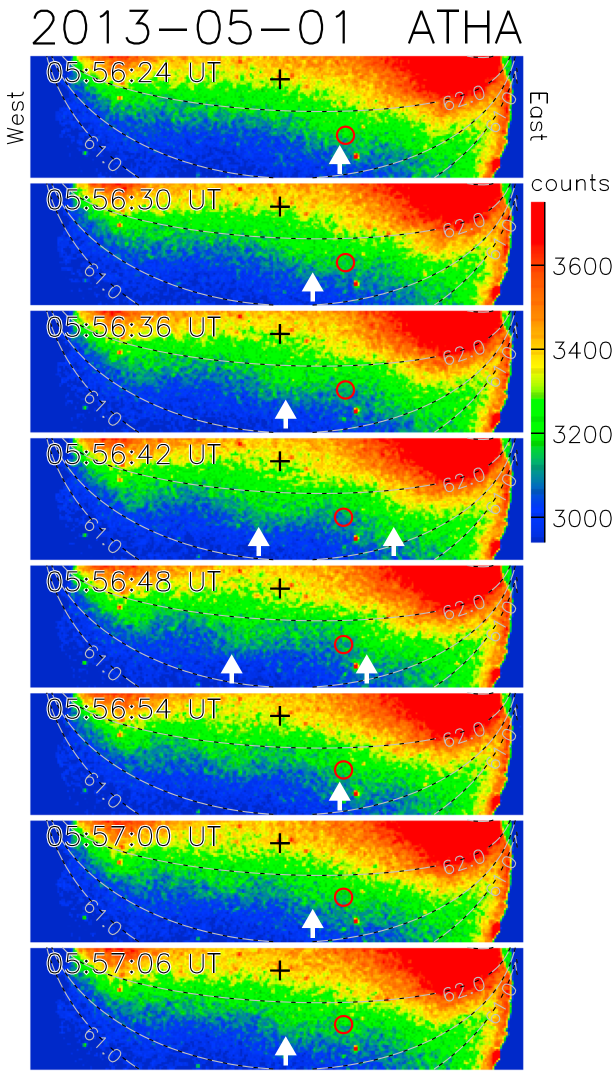

Figure 3. An example of auroral undulations observed with the ATHA ASI. The cropped images are displayed every 6 s during the interval of 05:56:24–05:57:06 UT. The images are smoothed with a 2 × 2 kernel to highlight the auroral undulation structures (white arrows). The black cross denotes the zenith of ATHA. The magnetic footprints at 110 km of the Van Allen Probe-B spacecraft are also overlaid by the red circle.

Examples of partial ASI images that captured the auroral undulations for 05:56:24–05:57:06 UT are shown in Figure 3, together with the RBSP-B footprint (red circle) given by the T96 model. Each of the eight images every 6 s, which was obtained from roughly the center quarter of the all-sky image, was smoothed by using a 2 × 2 kernel to highlight the undulation structure by reducing the high-frequency luminosity information. The noticeable undulations are marked by the white arrows to highlight their westward propagation. More detailed temporal evolution of the auroral undulations can be seen from Movie S1 in the supporting information.

In order to characterize the spatiotemporal behavior of the auroral undulations, Figures 4a–4e illustrate the time sequence of the latitudinal and longitudinal luminosity profiles for 05:48–05:58 UT, known as keogram (ewogram) produced from the ATHA ASI images along the south to north (west to east) cross section. The raw and detrended keograms are presented in Figures 4a and 4b, respectively. The detrended keogram was obtained by subtracting slower variations from the raw keogram with a 100 s high-pass filter. As seen in Figure 4a, a brighter region gradually shifted equatorward, eventually crossing the zenith of ATHA (horizontal dashed line at 62.2°). The equatorward boundary of the brighter region exactly corresponded to the equatorward edge of the diffuse auroral region on which the undulation structure was formed. Taking a close look at both keograms, a quasiperiodic luminosity variation is seen as a result of the successive passage of auroral undulations propagating westward over the zenith. Such a quasiperiodic signature is seen more clearly in Figure 4c, which is a high-pass filtered version of the auroral luminosity variations averaged in the latitude range of 61.75° to 62.50° of the keogram. We identified the dominant period of the auroral luminosity variations to be ~40 s (25 mHz).

Figures 4d and 4e present the raw and detrended ewograms, respectively, as time series of the longitudinal auroral profile. The ewograms allow a visual inspection to more readily identify the quasiperiodic signature in the auroral luminosity. The quasiperiodic brightness signature in Figure 4e (shown as a stripe pattern) directly reflects the westward propagation of the auroral undulations. The average westward propagation speed, as estimated from the traces, ranged from 3 to 4 km s^{-1}, which corresponds roughly to a speed of ~30–45 km s^{-1} at the conjugate RBSP-B location.

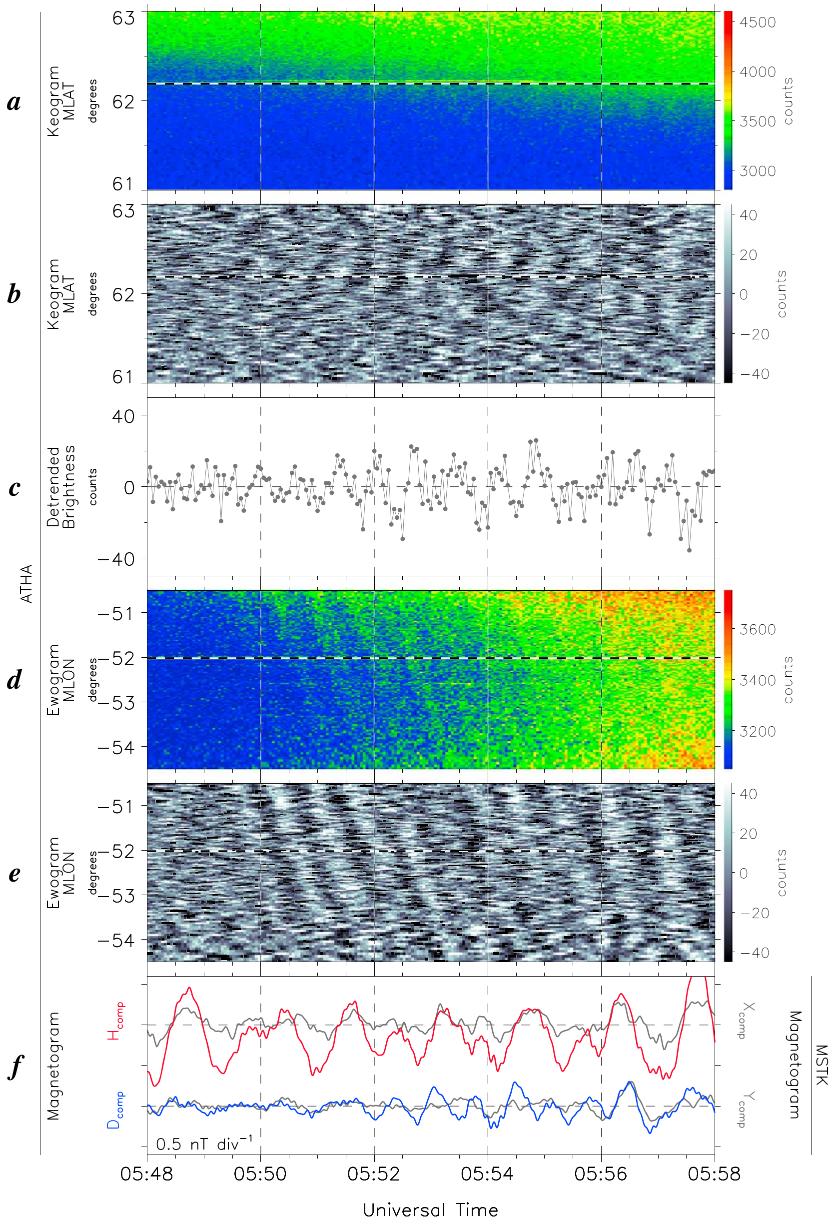

Figure 4. (a) Row keogram (north-south) along the magnetic longitude (MLON) of the zenith of ATHA during the interval of 05:48–05:58 UT on 1 May 2013. (b) Detrended keogram. (c) Detrended variation of auroral luminosity averaged over the latitude range between 61.75° and 62.50° of keogram. (d) Row ewogram (east-west) along the MLAT of the zenith at ATHA. (e) Detrended ewogram. The horizontal dashed line in keogram (ewogram) denotes the MLAT (MLON) at the zenith of ATHA. (f) The 100 s high-pass filtered magnetic field variations in the horizontal components at ATHA (color-coded curves) and MSTK (gray curves).

The optical data can provide a direct determination of the azimuthal wave number (m) and wavelength (λ) without any theoretical assumptions, as well as the propagation speed. For this event, the m number and wavelength of the quasiperiodic luminosity variations were estimated from the spatiotemporal signature of the auroral undulations to be $m \sim -103$ (here negative m is taken to represent westward phase propagation) and $\lambda \sim 180$ km in the ionosphere (~2000 km in the magnetosphere), respectively. The high-m signature seen in the auroral undulations appears to be analogous to the ionospheric measurement of high-m (~100) ULF waves with an HF sounder during the Doppler Pulsation Experiment [*Yeoman et al.*, 2000].

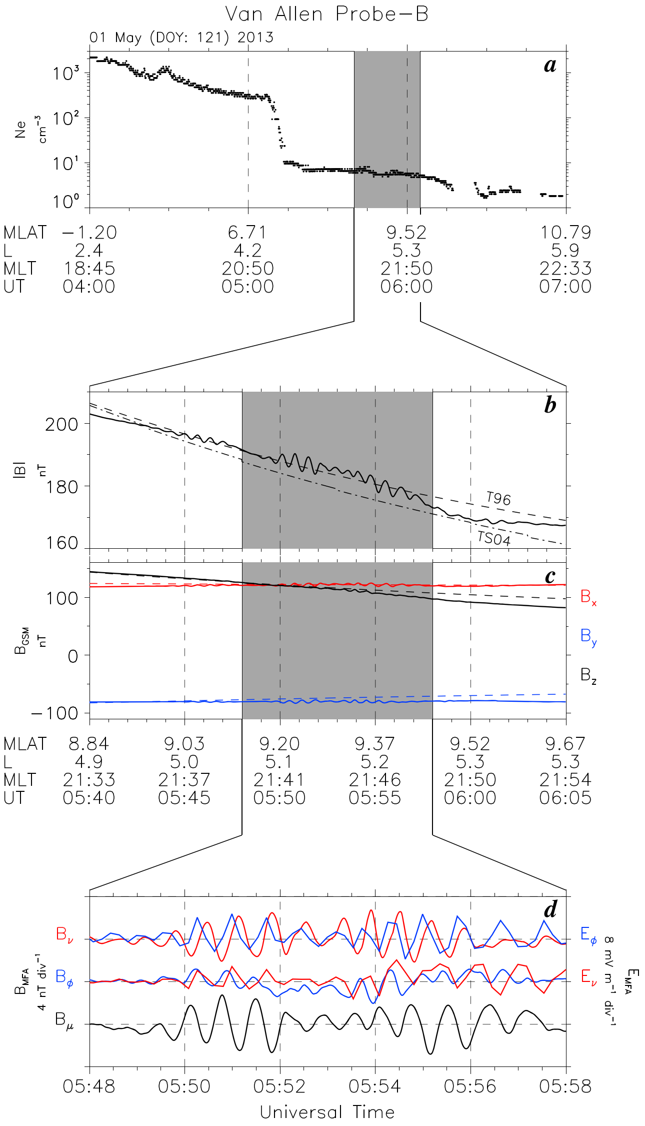

Figure 5. (a) Electron density at the Van Allen Probe-B spacecraft for 04:00–07:00 UT on 1 May 2013. (b) Magnetic field strength for 05:40–06:05 UT, together with the T96 (dashed curve) and TS04 (dash-dotted curve) model fields. (c) Magnetic field vector (B_x: red, B_y: blue, and B_z: black) in GSM coordinates. Each component of only the T96 model magnetic field is also drawn by dashed curve as a reference. (d) Magnetic field (B_ν, B_φ, and B_μ) and electric field (E_ν and E_φ) vectors in MFA coordinates for the zoomed in interval from 05:48 to 05:58 UT.

Theoretically, in general, most high-*m* ULF waves propagating from the magnetosphere to ground level are expected to be attenuated at the ground because of ionospheric screening [*Hughes and Southwood*, 1976]. The 100 s high-pass filtered magnetograms from ATHA and MSTK are shown in Figure 4f. Contrary to the shielding expectation, the corresponding (to the auroral luminosity variation) magnetic field oscillations were found only in the *D* component of the magnetic field at ATHA, in particular for 05:52–05:56 UT. At least for this interval, the *D*-component magnetic pulsations were apparently correlated with the auroral luminosity oscillations.

At MSTK, which was located ~1.0° equatorward of ATHA, on the other hand, similar magnetic field oscillations were less evident. However, it is interesting to note that the *Y*-component (east) variations of the geomagnetic field at MSTK appeared to become progressively similar to the *D*-component variation at ATHA, as the auroral undulations were approaching MSTK. This implies that the magnetic pulsations on the ground were likely associated with ionospheric conductivity variations modulated by diffuse particle precipitation in association with the westward passage of the auroral undulations [cf. *Buchert et al.*, 1999].

3.3. Conjugate Observations in the Inner Magnetosphere

During the interval of interest (05:45–06:00 UT), RBSP-B was outbound in its orbit from $(x, y, z) = (-4.0, 2.9, 0.8\ R_E)$ to $(-4.3, 2.7, 0.9\ R_E)$ in the solar magnetic coordinates (see Figures 1a and 1b), i.e., at the radial distance of ~5.0 R_E, in the premidnight sector (~21:45 MLT), and off the equatorial plane (~9.3° north from the equatorial plane).

To identify where RBSP-B was located relative to the plasmapause, the electron density profile determined from EMFISIS plasma wave spectra throughout the overall RBSP-B outbound orbit from 04:00 to 07:00 UT is shown in Figure 5a. Around 05:15 UT when the outbound orbit was near the radial distance of ~4.5 R_E, RBSP-B observed a steep drop in the electron density from ~300 cm^{-3} to ~10 cm^{-3}. The electron density further decreased to ~6 cm^{-3} during the interval of interest (gray shading) in which RBSP-B was at the radial distance of ~5.0 R_E. The interval of good magnetic conjunction of RBSP-B with the auroral undulations observed at ATHA occurred outside the plasmapause.

The EMFISIS magnetic field measurements from RBSP-B between 05:40 and 06:05 UT are shown in Figures 5b and 5c. In Figure 5b, the observed total magnetic field ($|B|$) is compared with the T96 (dashed curve) and TS04 (dash-dotted curve) model predictions. During the interval of interest, the T96 model performance seemed slightly better than the TS04 one (an underestimation by up to ~5 nT) for the prediction of $|B|$ at RBSP-B. Superimposed on Figure 5c is each component of the T96 model magnetic field (dashed curve). It is found that all components of the T96 model magnetic field were generally in agreement with those of the observed magnetic field, except for a small difference (within ~10–20 nT) in B_y and B_z after 05:55 UT. Such a good agreement between the observed and modeled magnetic fields at RBSP-B guarantees a certain level of reliability of the predicted ionospheric footprint traced from RBSP-B along a field line (Figure 1c). This also allows us to make a reliable comparison of the auroral undulation signatures during the period of interest with the spacecraft measurements from the inner magnetospheric source region.

It is worth noting that while for B_y and B_z both model predictions were almost the same (TS04 outputs not shown here), the T96 model prediction of B_x was better than TS04 like $|B|$. Based on the model outputs compared with the RBSP-B magnetic field observations, it would be reasonable to expect that T96 had slightly better performance for the RBSP-B footprint prediction during this event.

3.4. Magnetospheric ULF Waves

From 05:40 to 06:05 UT, the total magnetic field decreased gradually from ~200 nT to ~170 nT (Figure 5b). Around 05:50 UT, the dominant component of the magnetic field made a switch from B_z to B_x (Figure 5c), resulting from a topological change of the premidnight inner magnetosphere from dipole-like field line to more stretched field line that progressed during the substorm growth phase.

On the stretched field lines, RBSP-B observed a monochromatic magnetic field oscillation in all components, particularly noticeable during the interval of 05:48–05:58 UT when the auroral undulations (luminosity oscillations) were observed in the conjugate ionosphere (Figure 4). The magnetic field oscillations can be interpreted as a sign of magnetospheric ULF waves. In this study, we primarily focused on this 10 min interval (05:48–05:58 UT; gray shading) for the ULF wave analyses.

The temporal variations of the **B** and **E** vectors for 05:48–05:58 UT are presented in Figure 5d using the MFA coordinates. The poloidal (B_ν, E_φ), toroidal (B_φ, E_ν), and compressional (B_μ) components of the magnetospheric ULF waves are shown from the top. Both **B** and **E** show stronger poloidal oscillations than toroidal components. The E_φ oscillations had a peak to peak amplitude of 5–10 mV m^{-1}. Such a strong E_φ oscillation resembles that of the dawnside fundamental poloidal waves (E_φ~10 mV m^{-1}, peak to peak) at L~5.2 reported by *Dai et al.* [2013]. The peak to peak amplitude of B_ν was ~4 nT, being ~2% of the background magnetic field. The phase of B_ν lagged E_φ by ~90°, which indicates that the poloidal oscillations were associated with a standing Alfvén wave. Furthermore, because the spacecraft was northward of the magnetic equator, the observed phase delay indicates that the standing wave had a second harmonic mode structure (a fundamental mode would have produced the opposite phase delay) [*Singer et al.*, 1982].

A spectral analysis giving a more quantitative inspection of the **B** and **E** waveforms was carried out, and the results are summarized in Figure 6. As is evident in Figures 6a and 6b, all components of the **B** and **E** fields for 05:50–05:56 UT exhibited a strong spectral power at 25.4 mHz, in good agreement with that of the auroral luminosity oscillations shown in Figure 4. The spectral analysis also confirms that the poloidal mode was the most significant component during this event. Figure 6c shows the phase relationship between the **B** and **E** fields for both poloidal and toroidal waves. The cross phase results are displayed only when the coherency is greater than 0.8. The cross phase result for the poloidal mode indicated that B_ν lagged E_φ by ~60°–90°, supporting the visual inspection. For the toroidal mode, B_φ led E_ν by ~45°–80°. Both the **E-B** phase relationships provide strong evidence that the poloidal and toroidal waves were a second harmonic mode structure along the background magnetic field, as illustrated schematically in Figure 7.

There is additional evidence for the second harmonic mode in terms of the (magnetoseismic) relationship between the wave frequency and plasma density. From a numerical calculation of the second harmonic frequency using the guided poloidal wave equation of *Cummings et al.* [1969] for the dipole field line at $L = 5.2$ and mass density given by $\rho = \rho_{\mathrm{eq}}(LR_E/R)^{-1}$, we find that the observed frequency of ~25 mHz corresponds to $\rho_{\mathrm{eq}} = 22$ amu cm^{-3}. Here ρ_{eq} is the equatorial mass density and R is the geocentric distance to the field line. Meanwhile, the electron number density n_e was ~6 cm^{-3} during the wave event (Figure 5a), which gives an average ion mass M ($=\rho/n_e \sim \rho_{eq}/n_e$) of ~4 amu. In the terrestrial magnetosphere, M lies somewhere between 1 amu (all-H^+ plasma) and 16 amu (all-O^+ plasma), with a typical plasmatrough value of ~4 amu [*Takahashi et al.*, 2006]. Therefore, the assumption of the second harmonic gives mass density and M estimates that are quite reasonable.

We show in Figure 8 the mode structure of the second harmonic wave that was obtained from the same poloidal wave equation, which is relevant to the particle flux oscillations at RBSP-B that is described in section 3.5. For the illustrative purpose, the electric field amplitude is chosen to be 10 mV m^{-1} at the RBSP-B position during the wave event. The corresponding B_ν amplitude is 9.5 nT, and ξ_ν radial displacement is ~270 km.

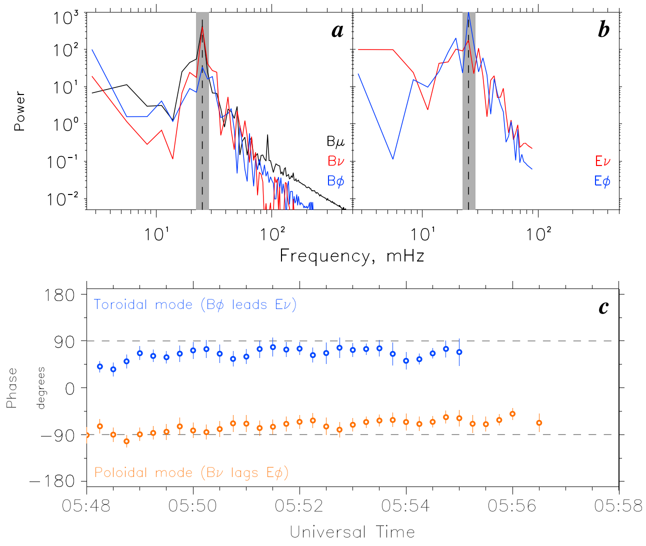

Figure 6. (a) Power spectra of **B** (B_ν, B_φ, and B_μ) in MFA coordinates for 05:50–05:56 UT. (b) Power spectra of **E** (E_ν and E_φ). (c) Temporal variations of phase of E_φ (E_ν) with respect to B_ν (B_φ) for the poloidal (toroidal) mode. The phases and their error bars are displayed only when coherence is higher than 0.8.

Up to now, we have ignored the compressional component of the magnetic field oscillations. The compressional component is in fact comparable to the radial component (Figure 5d) and implies that the cold plasma approximation that we used above is not adequate when discussing the generation mechanism of the wave. We do not elaborate on the mechanism but point out that many studies have reported compressional ULF waves in the magnetosphere, and our event is similar to them in many aspects, especially the second harmonic mode structure [e.g., *Hughes et al.*, 1978; *Takahashi et al.*, 1987], and that theoretical studies generally predict that second harmonic waves are preferentially excited in the ring current with free energy provided by either high-beta plasma or energetic ions [*Southwood*, 1976; *Chen and Hasegawa*, 1991; *Cheng et al.*, 1994].

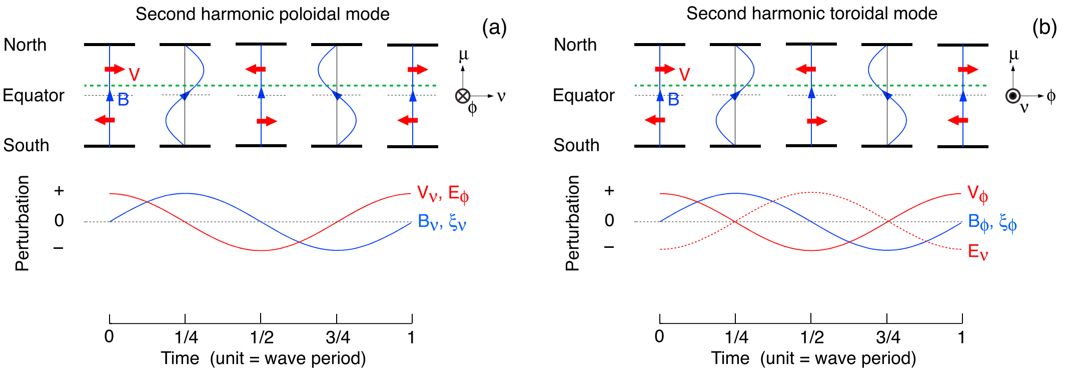

Figure 7. (a) The upper part shows snapshots of the field line pattern (blue curve with arrowhead) and plasma bulk velocity at the equator (red arrow) for a second harmonic poloidal mode field line oscillation in the magnetic meridian plane. Note that the radial (azimuthal) component in the upper left (right) part is right-hand direction, while the azimuthal (radial) component is directed inward (outward) perpendicular to the plane of this figure. The lower part shows the corresponding time series plots of the azimuthal (eastward) component of the electric field E_φ, radial (outward) component of the velocity V_ν, radial component of the magnetic field B_ν, and radial displacement of the field line ξ_ν measured at a fixed point in space slightly north of the magnetic equator (green dashed line). (b) Same as Figure 7a but for a second harmonic toroidal mode oscillation. For the second harmonic poloidal (toroidal) mode oscillation, the B oscillation lags (leads) the E oscillation.

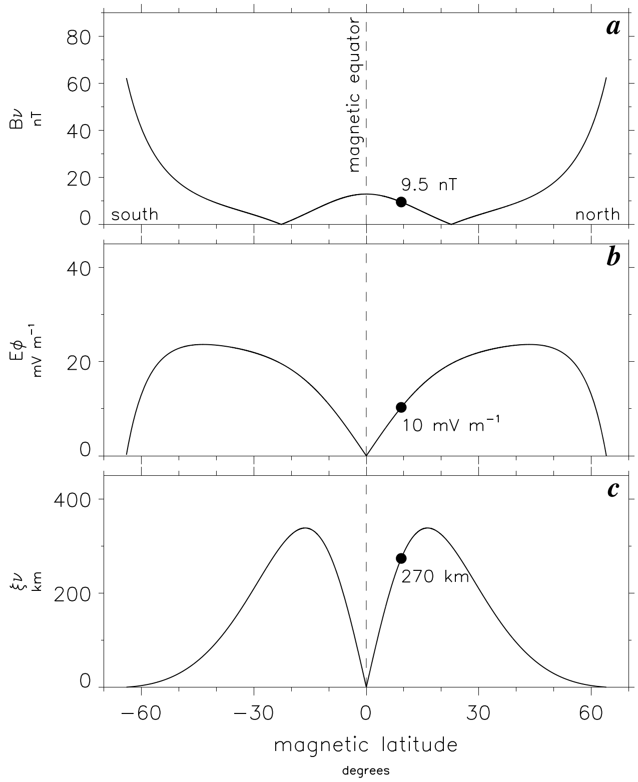

Figure 8. Theoretical structure of a second harmonic poloidal wave. The structure was obtained by solving the guided poloidal wave equation of *Cummings et al.* [1969] for $L = 5.2$, equatorial mass density of 22.4 amu cm^{-3}, and field line mass density variation proportional to R^{-1}, where R is the geocentric distance to the magnetic field line. The electric field amplitude is set to 10 mV m^{-1} at the satellite position of MLAT = 9.3° (shown by a solid circle). (a) Radial component of the magnetic field. (b) Azimuthal component of the electric field. (c) Radial displacement of the field line.

3.5. Interactions of Energetic Particles With ULF Waves

The poloidal waves at RBSP-B were accompanied by oscillations of the flux of both protons and electrons. Figure 9 presents omnidirectional differential fluxes of the RBSPICE 10–500 keV protons and MagEIS 30–500 keV electrons for 05:40–06:05 UT. The proton energy-time spectrogram exhibits the ULF-related modulation in the energy range from several tens of keV to a few hundreds of keV. To confirm wave-particle interactions through drift-bounce resonance that can drive the second harmonic poloidal wave, further details on the proton flux modulation are examined below in terms of the proton pitch angle dependence.

3.5.1. Proton Flux Modulation

Using data from the Active Magnetospheric Particle Tracer Explorers (AMPTE) CCE spacecraft near the magnetic equator, *Takahashi et al.* [1990] experimentally identified ion modulation behavior by a second harmonic poloidal wave, as expected from theoretical bounce resonance interactions [*Southwood et al.*, 1969]. In particular, it is well known that particle modulations strongly depend on pitch angle. The two main features expected are as follows: (1) ion flux modulations will tend to strengthen near-field-aligned directions and weaken near the perpendicular direction and (2) ion flux oscillations are expected to be out of phase between pitch angles, α and 180°–α.

In order to assess these features for this ULF wave event, an example is presented in Figure 10 using the 21.0–28.0 keV proton flux data acquired from the RBSPICE Time of Flight by Pulse Height proton product [*Mitchell et al.*, 2013]. This energy channel was selected based upon the theoretically expected ion resonance energy. The time sequence of the detrended proton flux, $\delta(\log j_H)$, as a function of pitch angle and time for 05:52–05:57 UT is shown in Figure 10a. The detrended flux was defined as $\delta(\log j_H) \sim \delta j_H / \langle j_H \rangle = (j_H - \langle j_H \rangle)/\langle j_H \rangle$ [cf. *Takahashi et al.*, 1990], where j_H is the differential flux observed in a given energy channel and $\langle j_H \rangle$ is a 200 s running mean of j_H. Positive (negative) perturbations appear in green (purple), and their colors are toward white as the amplitude diminishes. The time sequence of $\delta(\log j_H)$ at three pitch angles ($\alpha = 0°$: red, $\alpha = 90°$: light gray, and $\alpha = 180°$: blue) is displayed in Figure 10b. Figure 10c presents the radial component perturbation of the magnetic field (B_ν) for a comparison.

Throughout this interval, it is evident that the proton flux oscillations coincided with the B_ν oscillation. The $\delta(\log j_H)$ oscillation for 05:52–05:55 UT was most significant at $\alpha = 180°$, although it was moderate at $\alpha = 90°$. In this event, no clear phase reversal between the $\delta(\log j_H)$ oscillations at $\alpha = 0°$ and $\alpha = 180°$ was found. This feature was also found in the other tens of keV proton channels of the RBSPICE measurements. Although the in situ field measurements favor a conventional process that generates a second harmonic poloidal wave in the inner magnetosphere, the expected bounce resonance interactions are not evident from the particle measurements. This may arise from the fact that RBSP-B was slightly off the equatorial plane (~9°) and/or the fact that the field lines at RBSP-B were stretched tailward, although the exact explanation remains elusive.

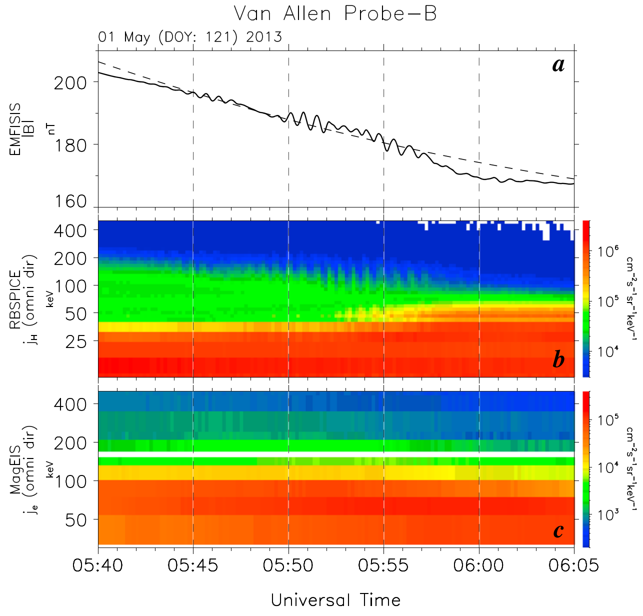

Figure 9. An overview of omnidirectional proton (j_H) and electron (j_e) fluxes from the Van Allen Probe-B spacecraft for 05:40–06:05 UT on 1 May 2013. (a) Magnetic field strength variation, same as in Figure 5b. (b) Proton flux in the 10–500 keV range acquired from the RBSPICE instrument. (c) Electron flux in the 30–500 keV range from the MagEIS instrument.

The attention herein has primarily been paid to the tens of keV proton flux modulations. However, the ULF-related modulations were also observed in the higher-energy proton fluxes as well as in energetic helium ion fluxes. The response of different ion species to the ULF waves is an important topic to be addressed in a future paper.

3.5.2. Electron Flux Modulation

Although electron flux modulations are barely seen in the omnidirectional spectrogram (Figure 9c), modulation is evident when the sectored data shown in Figure 11 are examined. Figure 11a shows the MagEIS electron flux in the 31.9 keV channel for 05:48–05:58 UT, averaged in two pitch angle bins, one centered at $\alpha = 0°$ (red line) and the other at $\alpha = 90°$ (gray line). The omnidirectional flux (black line) is also shown for a comparison. Figure 11b shows the detrended electron flux

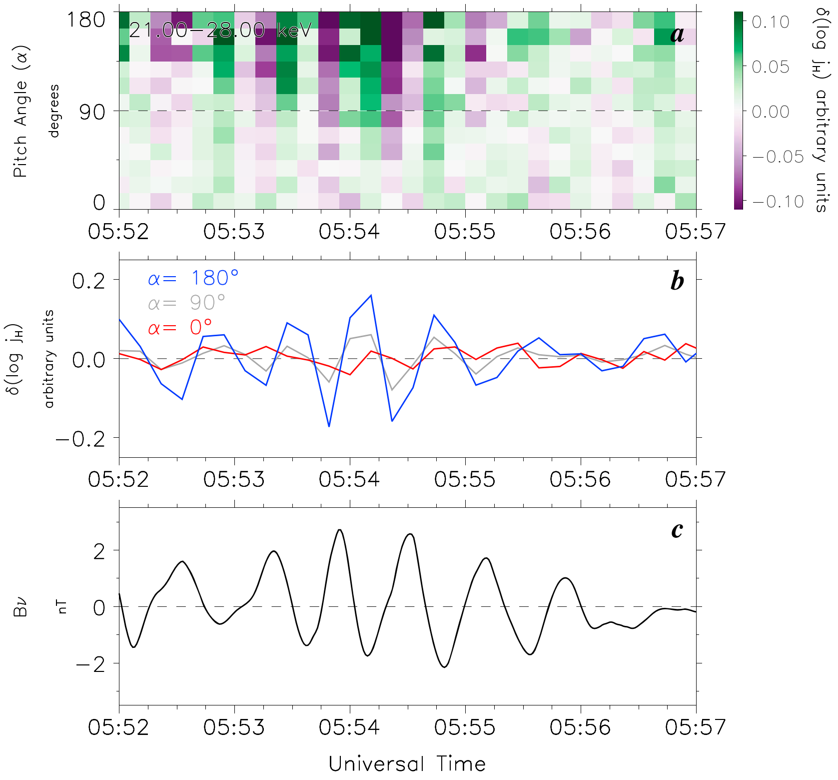

Figure 10. A comparison between proton flux and magnetic field data for the interval of 05:52–05:57 UT when poloidal ULF oscillation was significant. (a) Detrended proton flux, $\delta(\log j_H)$, at the 21.0–28.0 keV channel as a function of time and pitch angle. (b) Temporal variations of $\delta(\log j_e)$ at three different pitch angles, 0° (red line), 90° (gray line), and 180° (blue line). (c) The radial component (B_ν) of the magnetic field.

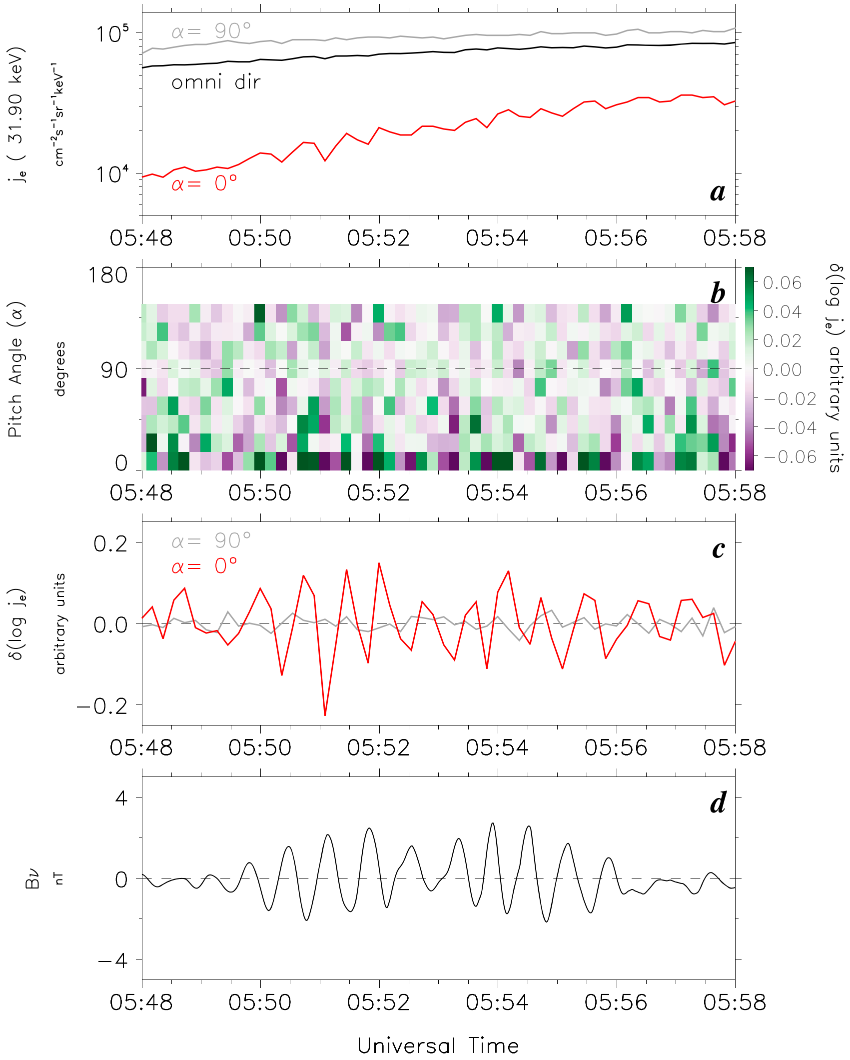

Figure 11. An example of electron flux (31.9 keV) modulation by magnetospheric ULF waves. (a) The omnidirectional (black line), parallel ($\alpha = 0°$, red line), and perpendicular ($\alpha = 90°$, gray line) electron fluxes, j_e; (b) pitch angle distribution of the high-pass filtered electron flux, $\delta(\log j_e)$; (c) temporal variations of $\delta(\log j_e)$ at two pitch angles, $\alpha = 0°$ (red line) and 90° (gray line); and (d) radial component (B_ν) of the magnetic field are shown from the top. Note that the detrended electron flux data at two pitch angle channels ($\alpha > 147°$) were removed owing to substantial data gaps.

variations in all available pitch angle bins for the same energy channel (there were no observations in sectors covering $\alpha > 147°$). The detrended electron fluxes $\delta(\log j_e)$ are represented in a similar way to Figure 10a. Figure 11c shows the detrended electron fluxes at $\alpha = 0°$ and 90°, that is, a high-pass filtered version of the fluxes shown in Figure 11a. The radial component perturbation of the magnetic field (B_ν) is also shown in Figure 11d for a comparison.

Electron oscillations are clearly seen at $\alpha = 0°$ but not at $\alpha = 90°$. This can be understood by the oscillatory convection of the radial gradient of electron fluxes induced by the second harmonic poloidal wave. This scenario is based on the particle and magnetic field observations shown in Figure 11. First, we note that the background electron flux had a strong pitch angle dependence. In Figure 11a, we see that the electron flux at $\alpha = 90°$ was larger than at $\alpha = 0°$ and changed only by a small factor (20–30% increase) during the 10 min interval shown. In contrast, the flux at $\alpha = 0°$ increased by ~300%. Because the spacecraft was moving outward, this increase means an outward gradient of the flux, $\partial j_e/\partial L > 0$ (ignoring temporal variations). Second, flux oscillations are evident only at $\alpha = 0°$ (Figures 11a and 11c). Third, the flux oscillation at $\alpha = 0°$ is out of phase with the B_ν oscillation (Figures 11c and 11d).

From the schematic field line displacement snapshots and corresponding B_ν time series shown in Figure 7a, we find that at the RBSP-B position, the maximum positive (negative) B_ν perturbation occurs when the field line is displaced the farthest from (closest to) the Earth. According to this geometry, we predict that in the presence of a positive gradient $\partial j_e/\partial L > 0$, the spacecraft sees a negative perturbation in electron flux when δB_ν is positive, because it corresponds to a time when the field line was displaced outward, carrying lower electron flux with it. The opposite happens when δB_ν is negative. The mathematical expression of this effect is given by

$$\delta(\log j_e) \sim -(\xi_\nu/R_E)\partial(\log j_e)/\partial L, \tag{1}$$

where ξ_ν is the field line displacement and R_E is the Earth's radius. For electrons with $\alpha = 0°$, we find $\partial(\log j_e)/\partial L \sim 0.5/0.15 \sim 3.3$ from Figure 11a, and according to Figure 8, the peak to peak amplitude of the field line displacement ξ_ν corresponding to the observed E_φ perturbation of ~8 mV m^{-1} peak to peak (~05:51 UT) is ~220 km. Substituting these values into the right-hand side of equation (1), we get $\delta(\log j_e) \sim 0.11$ peak to peak. This is in good quantitative agreement with the perturbations of j_e ($\alpha = 0°$) shown in Figures 11a and 11c.

Although the RBSP-B Helium Oxygen Proton Electron (HOPE) instrument [*Funsten et al.*, 2013] provides lower energy electron flux data, the temporal resolution is ~22 s (about half of the period of the ULF wave event), which is too low to clearly identify the ULF-related modulation of lower energy electrons that was likely occurring.

3.6. Detailed Comparisons Between Auroral Undulations and ULF Waves

In order to provide more definitive evidence that the auroral undulations in the ionosphere were closely linked to the second harmonic poloidal waves in the conjugate inner magnetosphere, the detrended field-parallel electron fluxes $\delta(\log j_e)$ at four different energy channels of 31–102 keV and radial component (B_ν) of the magnetic field from RBSP-B are compared with the auroral luminosity variations at the RBSP-B footprints given by T96 (red curve) and TS04 (blue curve) from the ATHA ASI and magnetic *D* component from the ATHA magnetometer in Figure 12. To take into account small uncertainties in the magnetic field mapping by each of the T96 and TS04 models, the auroral luminosity at each time has been calculated by averaging over 5 × 5 pixels centered on a pixel closest to the RBSP-B footprint and then subtracting the longer-period variations (>100 s) from the time series data with a high-pass filter. This comparison forms the basis of our conclusion that spatiotemporal behavior of the auroral undulations in the ionosphere reflects the second harmonic poloidal waves detected in the conjugate magnetospheric source region.

As mentioned in section 3.3, while the T96 model prediction of the magnetic field at RBSP-B was slightly better than TS04, the temporal variations in auroral luminosity at the T96 footprint were generally similar to those at the TS04 footprint throughout most of the interval (Figure 12c). Perhaps this is because average longitudinal separation between the T96 and TS04 footprints was nearly comparable to one azimuthal wavelength λ of the auroral undulations.

Before 05:52 UT, the luminosity variation at the RBSP-B footprint tends to be out of phase with the B_ν oscillation at RBSP-B (Figures 12b and 12c) and in phase with the related electron flux modulation, especially at 31.9 keV (Figure 12a). After 05:52 UT, on the other hand, both phase relationships were reversed. Such a difference between the intervals before and after 05:52 UT may be due to some mismatch between the predicted and exact conjugate footprints. Nevertheless, periodic signatures in the auroral undulations appeared to be closely synchronized with the field and particle oscillations related to the second harmonic poloidal waves observed with the RBSP-B spacecraft that was magnetically conjugate to the auroral undulations.

Interestingly, the *D*-component oscillation of the magnetic field at ATHA was well correlated (correlation coefficient > 0.7) with the B_ν oscillation at RBSP-B, at least for 05:52–05:56 UT. Such a good correlation between the magnetic field oscillations on the ground and in space resembles reports of giant pulsations (Pgs) seen as the ground signature of poloidal waves in the magnetosphere [*Takahashi et al.*, 2011]. However, we note that the azimuthal wave number *m* derived from the auroral luminosity oscillations (see section 3.2) was $|m| \sim 103$, much larger than the typical azimuthal wave number ($m \sim 16–35$) of Pgs. Also, note that the

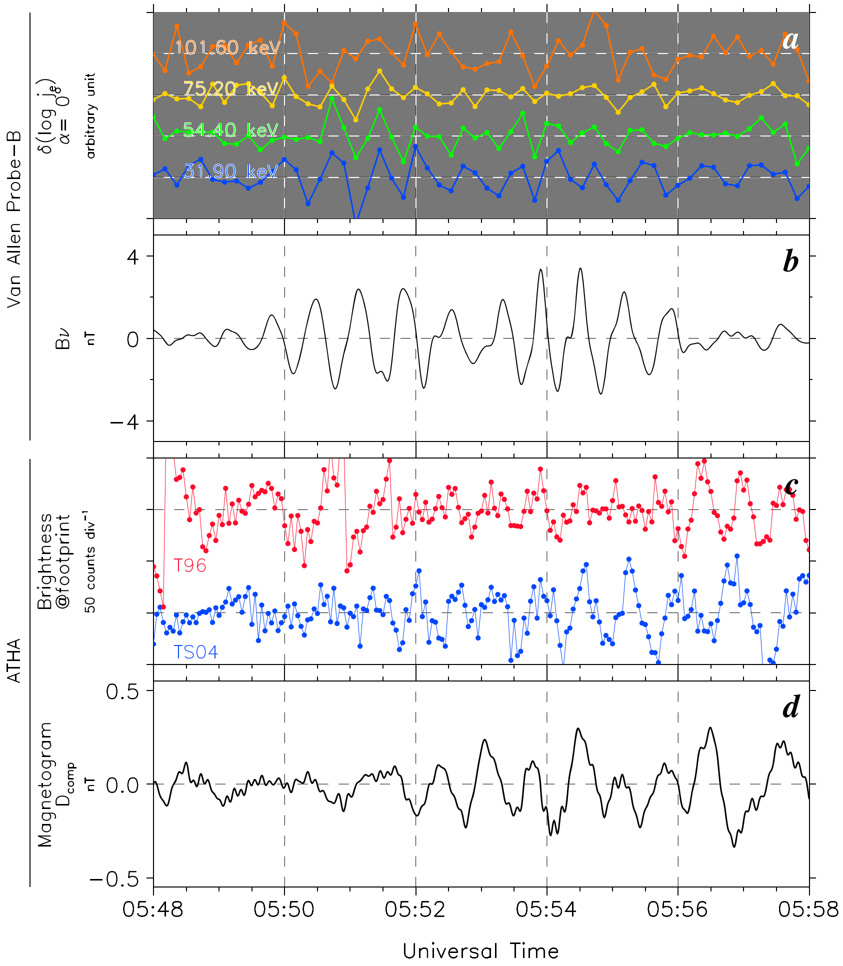

Figure 12. Detailed comparisons between key parameters obtained from the conjugate space-ground measurements at Van Allen Probe-B and ATHA. (a) Detrended field-aligned ($\alpha = 0°$) fluxes of energetic electrons, $\delta(\log j_e)$, at four different energy channels for 05:48–05:58 UT. (b) The radial component (B_ν) of the magnetic field. (c) Detrended variations of auroral luminosity at the Van Allen Probe-B footprints given by the T96 and TS04 models (see text for more details). (d) The *D* component of the high-pass filtered magnetic field variations at ATHA.

D-component oscillation had a very small amplitude (<0.5 nT peak to peak), much smaller than the typical amplitude (~10 nT) of Pgs.

4. Discussion

4.1. Summary of the Observations

We can summarize the simultaneous space-ground observations for the auroral undulation event on 1 May 2013 as follows:

1. The auroral undulation was observed with the ATHA ASI in the premidnight (~21:45 MLT) subauroral ionosphere in the course of the growth phase of a substorm.
2. The auroral undulation structure emerged equatorward of the equatorward shifting growth phase arc and propagated westward at a speed of ~3–4 km s^{-1}. The azimuthal wavelength was ~180 km in the ionosphere (~2000 km in the conjugate magnetosphere, i.e., the RBSP-B location), consistent with that reported in the previous ground studies.
3. The successive passage of the auroral undulations over an observing point yielded the quasiperiodic auroral luminosity oscillations with a period of ~40 s (25.0 mHz).

4. The spatial-temporal signature of the auroral undulations allowed us to directly estimate the azimuthal wave number, *m*, of the auroral luminosity oscillations, which were found to be $m{\sim}-103$.
5. RBSP-B, conjugate to the auroral undulations, observed intense poloidal ULF waves on tailward stretched field lines just outside the plasmapause. The dominant period was consistent with that of the auroral luminosity oscillations.
6. The nature of the poloidal waves was evident in strong oscillations in the radial magnetic field (~4 nT) and azimuthal electric field (~5–10 mV m^{-1}).
7. We identified the poloidal waves to be the second harmonic mode along the magnetic field line in terms of both the **E-B** phase relationship and the magnetoseismic relationship. It is interesting to note that the wave properties deduced from the auroral luminosity oscillations are also consistent with the theoretical predictions of a second harmonic poloidal wave by *Takahashi et al.* [1990].
8. The tens of keV proton flux modulation signatures around the resonant energy do not necessarily fit those expected from a bounce resonance interaction, perhaps due to the off-equatorial location of the RBSP-B measurements.
9. The tens of keV electron flux modulations can be interpreted in terms of an oscillatory convection of the radial gradient of electron fluxes induced by the second harmonic poloidal wave.
10. The ATHA ground-based magnetometer recorded fairly weak ($<$1 nT) but clear magnetic fieldoscillations in the *D* component, which was well correlated with the B_y oscillations at RBSP-B, as well as the auroral luminosity oscillations at its footprint.

4.2. Source of Auroral Undulations

The westward propagating auroral undulations presented here bear morphological analogy to previous auroral undulation events [*Lui et al.*, 1982; *Zhang et al.*, 2005; *Lewis et al.*, 2005; *Henderson et al.*, 2010], especially the ground-based optical features reported by *Nishitani et al.* [1994] and *Baishev et al.* [2012] in terms of wavelength and location. A major difference is that the propagation speed of our event was slightly faster than previous ground-based reports.

It has been suggested that duskside auroral undulations are caused by either a flow shear-related instability (such as KHI) at subauroral latitudes [*Lui et al.*, 1982; *Kelley*, 1986; *Yamamoto et al.*, 1993] or a drift wave instability in the magnetosphere [*Lui et al.*, 1982; *Fedorovich*, 1988; *Lewis et al.*, 2005]. However, it is not clear whether these instabilities lead to excitation of second harmonic poloidal waves in the magnetosphere.

Super Dual Auroral Radar Network (SuperDARN: http://vt.superdarn.org/tiki-index.php) radar measurements (not shown) near ATHA, on the other hand, observed a westward ionospheric flow of 300–450 m s^{-1} (corresponding to a northward electric field of ~25 mV m^{-1}) confined in ~59.5°–61.0° MLAT, ~1° equatorward of the auroral undulations. The narrow westward flow channel may meet a minimum background condition required for the development of the KHI there [*Yamamoto et al.*, 1993], although the observed flow speed (or electric field) was about half or less than that observed by polar-orbiting satellites [e.g., *Rich et al.*, 1980; *Kelley*, 1986; *Zhang et al.*, 2005]. Unfortunately, further evidence supporting the KHI mechanism was not found in available data sets.

Here we emphasize that the KHI mechanism is not the only possibility, as already described by many facts in mutual agreement between spatiotemporal signatures in the conjugate area of the premidnight magnetosphere and ionosphere. Despite the single-event analysis, the fruitful and very important conjugate space-ground observations allow us to propose an alternative scenario. That is, that the second harmonic poloidal waves in the inner magnetosphere act as a possible driver of auroral undulations in the duskside subauroral ionosphere. Their relationship to magnetic ULF waves bears some analogy to previous reports [*Baishev and Solovyev*, 1994, 1995; *Baishev et al.*, 1997, 2000], indicating good relationship between geomagnetic Pc5 pulsations on the ground and large-scale undulations on the evening diffuse auroral boundary, although the period and wavelength are different.

The westward propagation velocity of the auroral undulation with a speed of 3–4 km s^{-1} is faster than an average peak velocity of premidnight subauroral polarization streams (commonly known as "SAPS") for geomagnetically disturbed periods; for instance, the average velocity is not more than 1 km s^{-1} for *Kp*~3–5 near 22:00 MLT [cf., Figure 5 of *Foster and Vo*, 2002]. Two possibilities are suggested to explain the propagation speed. One possibility is that the undulation velocity is associated with an extremely high (up to ~2–3 km s^{-1}), localized ($<1°$) drift velocity in the evening subauroral region that occasionally occurs during geomagnetically active periods, which is known as subauroral ion drifts (SAID) [*Anderson et al.*, 1991] or polarization jet [*Galperin*, 2002] and comparable to electric fields of ~50–100 mV m^{-1} or more [e.g., *Rich et al.*, 1980; *Kelley*, 1986]. Around the interval of interest, the DMSP ion drift velocity measurements in the southern hemisphere (not shown here) gave an indirect but promising indication for the presence of westward ion velocity exceeding 1.0 km s^{-1}, although the DMSP observations were made at UT and MLT/MLAT that differed significantly from those of the auroral undulation we observed. Another possibility is that the undulation velocity is related to the magnetic field gradient and curvature drift of tens of keV protons. As mentioned in section 3.2, the speed of 3–4 km s^{-1} in the ionosphere corresponds to ~30–45 km s^{-1} in the conjugate magnetosphere, roughly comparable to the westward drift speed of tens of keV protons in the ring current region [*Yeoman et al.*, 2000]. Given that the second harmonic poloidal waves are the magnetospheric counterpart of the auroral undulation, the latter seems to be more reasonable.

4.3. Driver of Diffuse Electron Precipitation

From a magnetosphere-ionosphere coupling point of view, the most straightforward way to explain the observed diffuse-type auroral undulations in the ionosphere is that they are attributed to diffuse electron precipitation caused by the scattering of energetic electrons into the loss cone. Hence, we discuss here briefly what causes the diffuse precipitation of energetic electrons in terms of wave-particle interactions. Two possible mechanisms can be considered: one is the resonant interaction process of energetic electrons with ULF-modulated whistler mode chorus waves and the other is a potential interaction process of energetic electrons with second harmonic poloidal waves.

The former process is widely accepted as a typical generation mechanism involved in the modulation of diffuse precipitation of trapped energetic electrons [*Coroniti and Kennel*, 1970]. As a possible scenario, the compressional component of magnetospheric ULF magnetic field oscillations plays an effective role in modulating an existing chorus source in the magnetospheric equatorial plane. For our event, we found that the compressional component of the magnetic field at RBSP-B oscillated in phase with the tens of keV electron flux modulation. If some of the chorus waves mediated the interaction between the compressional magnetic field oscillation and electron modulation, then it can be expected that the coincident chorus wave modulation could also be detected with RBSP-B. To confirm or refute this possibility, dynamic spectra in the 5–10,000 Hz band recorded in the six-channel EMFISIS WaveForm Receiver (not shown here) of the RBSP-B EMFISIS instrument were examined. During the interval of interest, quasiperiodic modulation of 100–1000 Hz wave intensities (corresponding to lower band chorus: $0.1f_{ce} < f < 0.5f_{ce}$, where f_{ce} is the equatorial electron gyrofrequency) was detected in the electric field spectrogram but absent in the magnetic field spectrogram. Moreover, there appeared to be no one-to-one correspondence between the compressional magnetic field oscillations and 100–1000 Hz wave modulations. In the light of this result, it is unlikely to attribute at least the 100–1000 Hz wave intensity modulation in the electric field spectrogram as evidence of ULF-related chorus wave modulation. However, we cannot completely eliminate the chorus wave scattering process because RBSP-B at its off-equatorial plane location might not measure the actual wave-particle interaction.

On the other hand, could the energetic electrons interact with, and be scattered by, the second harmonic poloidal waves? In the course of their bounce motion, energetic electrons interact with the electric field of poloidal ULF waves, which can be considered stationary on the time scales of the bounce motion. The azimuthal component of the electric field leads to radial transport of electrons across their drift shells. Due to the widening of the atmospheric loss cone with a decrease in L, inward radial transport can transfer electrons into the loss cone leading to their subsequent precipitation in the atmosphere. Thus, poloidal waves can enhance the flux of precipitating electrons and therefore cause the observed undulations.

To verify this hypothesis, the amplitude (~100 km) of the undulations should be compared with the radial distance Δr in the ionosphere spanned by electrons during their motion from the equator to the ionosphere due to the influence of the E_φ oscillation. The radial distance is given by

$$\Delta r = \int_0^{T_b/4} u_r \;\; dt = c\int_0^{s_{\max}} \frac{E_\varphi}{B}\frac{1}{v\cdot\cos\alpha}ds, \tag{2}$$

where T_b is the bounce period, s is the distance along the field line, $s_{\max}$ is the field line length, u_r is the radial component of the electron $\mathbf{E}\times\mathbf{B}$ drift, E_φ is the poloidal mode ULF electric field, v is the electron velocity, α is the pitch angle, and B is the magnetic field intensity. Assuming the Earth's magnetic field to be dipolar, approximating the electric field distribution of the second harmonic poloidal wave along the field line as $E_\varphi = E_0 \sin(\pi s/s_{\max})$, taking the initial value of the electron pitch angle at 5°, and integrating numerically, we obtain the following estimate:

$$\Delta r = 5\cdot 10^{-3}\frac{E[\mathrm{mV/m}]}{\sqrt{K[\mathrm{keV}]}}L^4,\quad \mathrm{km}, \tag{3}$$

where E is the electric field, L is the L value, and K is the characteristic energy of energetic electrons.

Lewis et al. [2005] demonstrated an observational example that the diffuse precipitation of 1–10 keV electrons mainly contributed to the auroral emissions associated with large-scale undulations, using conjugate IMAGE–DMSP observations, in which a DMSP spacecraft skimmed along the edge of one of the large-scale undulations observed with the IMAGE FUV/Wideband Imaging Camera. Assuming the same characteristic energy and substituting the energy and the observed parameters ($L = 5.2$, $E = 10\ \mathrm{mV\,m^{-1}}$) into equation (3), we estimate Δr to be ~10–35 km. Although the radial distance in the ionosphere is a factor of ~3–10 smaller than the amplitude of the observed auroral undulations, this first-order estimation implies that this process can potentially be the source of energetic electrons responsible for the auroral undulations. Further work is required to confidently validate this hypothesis, in particular with numerical simulations as well as simultaneous, multipoint, in situ measurements for other examples of auroral undulations.

5. Conclusions

This paper has presented the premidnight auroral undulation event on 1 May 2013 observed by the THEMIS ASI at ATHA ($L = 4.6$), for which in situ field and particle measurements in the magnetosphere were simultaneously available from the RBSP-B spacecraft that was located just outside the plasmapause and conjugate to the auroral undulation. Such a good conjunction of the space-ground measurements has first allowed us to directly identify the magnetospheric driver of the auroral undulations. This case study has revealed that the auroral undulations were closely linked to the generation of second harmonic poloidal ULF waves.

Whereas we confirmed the morphological similarities between the magnetospheric and ionospheric phenomena, there still remains the question of what process is involved in the diffuse precipitation of energetic electrons responsible for the auroral undulations. The interaction of energetic electrons with the highly localized second harmonic poloidal ULF wave cannot be ruled out. This work also suggests that ground-based observations of auroral undulations in the premidnight subauroral ionosphere will offer new opportunities for remotely monitoring the structure and space-time dynamics of high-m ULF waves in the inner magnetosphere.

Acknowledgments
Work at JHU/APL was supported by the NASA grant (NNX14AB97G). The authors would like to thank the Van Allen Probes teams for operating the spacecraft and providing each instrument's data. The RBSPICE instrument was supported by JHU/APL subcontract 937836 to the New Jersey Institute of Technology under NASA prime contract no. NAS5–01072. G.I.K. was supported by the NASA grant NNX12AK09G and NSF grant AGS-1207445. The research at The University of Iowa was supported by JHU/APL contract no. 921647 under NASA prime contract no. NAS5–01072. The THEMIS GBO project is funded by NASA contract NAS5–02099 and supported by the Canadian Space Agency. For THEMIS ASI, we acknowledge the efforts of Harald Frey, Emma Spanwick, and Stephen Mende. Most of the data from the Van Allen Probe-B spacecraft used in this study are publicly available at CDAWeb (http://cdaweb.gsfc.nasa.gov/), while data from the THEMIS GBO measurements are available at the THEMIS mission website (http://themis.ssl.berkeley.edu/index.shtml). The RBSPICE proton flux data were obtained through the RBSPICE MIDL (http://sd-www.jhuapl.edu/rbspice/MIDL/), that is, a downloadable application developed for interactive analysis of the RBSPICE data. RBSP data are archived on the RBSPICE Science Data Center website: http://rbspice.ftecs.com/Data.html. The EFW electric field vector data in GSM coordinates were provided by L. Dai on request. The EMFISIS electron density data are available through the University of Iowa on request. The MSTK magnetometer data are publicly available from CARISMA (http://www.carisma.ca/) that is operated by the University of Alberta and funded by the Canadian Space Agency. The geomagnetic indices were obtained from WDC for geomagnetism, Kyoto. The OMNI solar wind data were obtained from the GSFC/SPDF OMNIWeb interface at http://omniweb.gsfc.nasa.gov.

Larry Kepko thanks Michael Henderson and another reviewer for their assistance in evaluating this paper.

References

Anderson, P. C., R. A. Heelis, and W. B. Hanson (1991), The ionospheric signatures of rapid subauroral ion drifts, *J. Geophys. Res.*, *96*(A4), 5785–5792, doi:10.1029/90JA02651.

Baishev, D. G., and S. I. Solovyev (1994), Characteristics of Pc1-2 and IPDP geomagnetic pulsations during large-scale undulations on the evening diffuse auroral boundary, *J. Geomagn. Geoelectr.*, *46*, 945–952.

Baishev, D. G., and S. I. Solovyev (1995), Characteristics of Pc1-2 and IPDP geomagnetic pulsations during formation of airglow undulations on the equatorward boundary of diffuse auroras in the evening sector, *Geomagn. Aeron., Engl. Transl.*, *35*, 171–177.

Baishev, D. G., K. Yumoto, S. I. Solovyev, N. E. Molochushkin, and E. S. Barkova (1997), Magnetic storm-time variations of the geomagnetic field during large-scale undulations of the evening diffuse aurora, *Geomagn. Aeron., Engl. Transl.*, *37*, 39–46.

Baishev, D. G., E. S. Barkova, S. I. Solovyev, K. Yumoto, M. J. Engebretson, and A. V. Koustov (2000), Formation of large-scale "giant" undulations at the equatorial boundary of diffuse aurora and Pc5 magnetic pulsations during the 14 January 1999 magnetic storm, in *Proc. 5th International Conference on Substorms*, pp. 427–430, ESA Publ., St. Petersburg, Russia.

Baishev, D. G., E. S. Barkova, and K. Yumoto (2012), Optical observations of large-scale undulations in the 23rd cycle of solar activity, *Geomagn. Aeron.*, *52*(2), 197–203.

Baker, K. B., and S. Wing (1989), A new magnetic coordinate system for conjugate studies at high latitudes, *J. Geophys. Res.*, *94*(A7), 9139–9143, doi:10.1029/JA094iA07p09139.

Blake, J. B., et al. (2013), The Magnetic Electron Ion Spectrometer (MagEIS) instruments aboard the Radiation Belt Storm Probes (RBSP) spacecraft, *Space Sci. Rev.*, *179*, 383–421, doi:10.1007/s11214-9991-8.

Buchert, S. C., R. Fujii, and K.-H. Glassmeier (1999), Ionospheric conductivity modulation in ULF pulsations, *J. Geophys. Res.*, *104*(A5), 10,119–10,133, doi:10.1029/1998JA900180.

Chen, L., and A. Hasegawa (1991), Kinetic theory of geomagnetic pulsations: 1. Internal excitation by energetic particles, *J. Geophys. Res.*, *96*(A2), 1503–1512, doi:10.1029/90JA02346.

Cheng, C. Z., Q. Qian, K. Takahashi, and A. T. Y. Lui (1994), Ballooning-mirror instability and internally driven Pc4-5 wave events, *J. Geomagn. Geoelectr.*, *46*, 997–1009.

Coroniti, F. V., and C. F. Kennel (1970), Electron precipitation pulsations, *J. Geophys. Res.*, *75*(7), 1279–1289, doi:10.1029/JA075i007p01279.

Cummings, W. D., R. J. O'Sullivan, and P. J. Coleman Jr. (1969), Standing Alfvén waves in the magnetosphere, *J. Geophys. Res.*, *74*(3), 778–793, doi:10.1029/JA074i003p00778.

Dai, L., et al. (2013), Excitation of poloidal standing Alfvén waves through drift resonance wave-particle interaction, *Geophys. Res. Lett.*, *40*, 4127–4132, doi:10.1002/grl.50800.

Fedorovich, G. V. (1988), The wave structure of the equatorial boundary of the zone of diffuse precipitation of auroral electrons, *Geomagn. Aeron., Engl. Transl.*, *28*, 83–87.

Foster, J. C., and H. B. Vo (2002), Average characteristics and activity dependence of the subauroral polarization stream, *J. Geophys. Res.*, *107*(A12), 1475, doi:10.1029/2002JA009409.

Funsten, H. O., et al. (2013), Helium, Oxygen, Proton, and Electron (HOPE) mass spectrometer for the Radiation Belt Storm Probes mission, *Space Sci. Rev.*, *179*, 423–484, doi:10.1007/s11214-013-9968-7.

Galperin, Y. I. (2002), Polarization jet: Characteristics and a model, *Ann. Geophys.*, *20*, 391–404.

Henderson, M. G., E. F. Donovan, J. C. Foster, I. R. Mann, T. J. Immel, S. B. Mende, and J. B. Sigwarth (2010), Start-to-end global imaging of a sunward propagating, SAPS-associated giant undulation event, *J. Geophys. Res.*, *115*, A04210, doi:10.1029/2009JA014106.

Hughes, W. J., and D. J. Southwood (1976), The screening of micropulsation signals by the atmosphere and ionosphere, *J. Geophys. Res.*, *81*(19), 3234–3240, doi:10.1029/JA081i019p03234.

Hughes, W. J., D. J. Southwood, B. Mauk, R. L. McPherron, and J. N. Barfield (1978), Alfvén waves generated by an inverted plasma distribution, *Nature*, *275*, 43–45, doi:10.1038/275043a0.

Kelley, M. C. (1986), Intense sheared flow as the origin of large-scale undulations of the edge of the diffuse aurora, *J. Geophys. Res.*, *91*(A3), 3225–3230, doi:10.1029/JA091iA03p03225.

Kletzing, C. A., et al. (2013), The Electric and Magnetic Field Instrument Suite and Integrated Science (EMFISIS) on RBSP, *Space Sci. Rev.*, *179*, 127–181, doi:10.1007/s11214-013-9993-6.

Lewis, W. S., J. L. Burch, J. Goldstein, W. Horton, J. C. Perez, H. U. Frey, and P. C. Anderson (2005), Duskside auroral undulations observed by IMAGE and their possible association with large-scale structures on the inner edge of the electron plasma sheet, *Geophys. Res. Lett.*, *32*, L24103, doi:10.1029/2005GL024390.

Lui, A. T. Y., C. I. Meng, and S. Ismail (1982), Large amplitude undulations on the equatorward boundary of the diffuse aurora, *J. Geophys. Res.*, *87*(A4), 2385–2400, doi:10.1029/JA087iA04p02385.

Mann, I. R., et al. (2008), The upgraded CARISMA magnetometer array in the THEMIS era, *Space Sci. Rev.*, *141*, 413–451, doi:10.1007/s11214-008-9457-6.

Mauk, B. H., N. J. Fox, S. G. Kanekal, R. L. Kessel, D. G. Sibeck, and A. Ukhorskiy (2013), Science objectives and rationale for the radiation belt storm probes mission, *Space Sci. Rev.*, *179*, 3–27, doi:10.1007/s11214-012-9908-y.

Mende, S. B., S. E. Harris, H. U. Frey, V. Angelopoulos, C. T. Russell, E. Donovan, B. Jackel, M. Greffen, and L. M. Peticolas (2008), The THEMIS array of ground-based observatories for the study of auroral substorms, *Space Sci. Rev.*, doi:10.1007/s11214-008-9380-x.

Mitchell, D. G., et al. (2013), Radiation Belt Storm Probes Ion Composition Experiment (RBSPICE), *Space Sci. Rev.*, *179*, 263–308, doi:10.1007/s11214-013-9965-x.

Nishitani, N., G. Hough, and M. W. J. Scourfield (1994), Spatial and temporal characteristics of giant undulations, *Geophys. Res. Lett.*, *21*(24), 2673–2676, doi:10.1029/94GL02240.

Rich, F. J., W. J. Burke, M. C. Kelley, and M. Smiddy (1980), Observations of field-aligned currents in association with strong convection electric fields at subauroral latitudes, *J. Geophys. Res.*, *85*(A5), 2335–2340, doi:10.1029/JA085iA05p02335.

Singer, H. J., J. W. Hughes, and C. T. Russell (1982), Standing hydromagnetic waves observed by ISEE 1 and 2: Radial extent and harmonic, *J. Geophys. Res.*, *87*(A5), 3519–3529, doi:10.1029/JA087iA05p03519.

Southwood, D. J. (1976), A general approach to low-frequency instability in the ring current plasma, *J. Geophys. Res.*, *81*(19), 3340–3348, doi:10.1029/JA081i019p03340.

Southwood, D. J., J. W. Dungey, and R. J. Etherington (1969), Bounce resonant interactions between pulsations and trapped particles, *Planet. Space Sci.*, *17*, 349–361.

Takahashi, K., J. F. Fennell, E. Amata, and P. R. Higbie (1987), Field-aligned structure of the storm time Pc5 wave of November 14–15, 1979, *J. Geophys. Res.*, *92*(A6), 5857–5864, doi:10.1029/JA092iA06p05857.

Takahashi, K., R. W. McEntire, A. T. Y. Lui, and T. A. Potemra (1990), Ion flux oscillations associated with a radially polarized transverse Pc 5 magnetic pulsation, *J. Geophys. Res.*, *95*(A4), 3717–3731, doi:10.1029/JA095iA04p03717.

Takahashi, K., R. E. Denton, R. R. Anderson, and W. J. Hughes (2006), Mass density inferred from toroidal wave frequencies and its comparison to electron density, *J. Geophys. Res.*, *111*, A01201, doi:10.1029/2005JA011286.

Takahashi, K., K.-H. Glassmeier, V. Angelopoulos, J. Bonnell, Y. Nishimura, H. J. Singer, and C. T. Russell (2011), Multisatellite observations of a giant pulsation event, *J. Geophys. Res.*, *116*, A11223, doi:10.1029/2011JA016955.

Tsyganenko, N. A. (1989), A magnetospheric magnetic field model with a warped tail current sheet, *Planet. Space Sci.*, *37*, 5–20.

Tsyganenko, N. A., and M. I. Sitnov (2005), Modeling the dynamics of the inner magnetosphere during strong geomagnetic storms, *J. Geophys. Res.*, *110*, A03208, doi:10.1029/2004JA010798.

Tsyganenko, N. A., and D. P. Stern (1996), Modeling the global magnetic field of the large-scale Birkeland current systems, *J. Geophys. Res.*, *101*(A12), 27,187–27,198, doi:10.1029/96JA02735.

Wygant, J. R., et al. (2013), The Electric Field and Waves instruments on the Radiation Belt Storm Probes mission, *Space Sci. Rev.*, *179*, 183–220, doi:10.1007/s11214-013-0013-7.

Yamamoto, T., K. Makita, and C.-I. Meng (1993), A particle simulation of "giant" undulations on the evening diffuse auroral boundary, *J. Geophys. Res.*, *98*(A4), 5785–5800, doi:10.1029/92JA01434.

Yeoman, T. K., D. M. Wright, P. J. Chapman, and A. B. Stockton-Chalk (2000), High-latitude observations of ULF waves with large azimuthal wave numbers, *J. Geophys. Res.*, *105*(A3), 5453–5462, doi:10.1029/1999JA005081.

Zhang, Y., L. J. Paxton, D. Morrison, A. T. Y. Lui, H. Kil, B. Wolven, C.-I. Meng, and A. B. Christensen (2005), Undulations on the equatorward edge of the diffuse proton aurora: TIMED/GUVI observations, *J. Geophys. Res.*, *110*, A08211, doi:10.1029/2004JA010668.